Hybrid Navigation of Omnidirectional AMRs Using Dynamic Control and FWNN-BLS Compensation

Ching-Chih Tsai, *Fellow, IEEE*, Chi-Hsiang Li, Jia-Wei Su, Shih-Che Chen

***Abstract*—This paper proposes a novel hybrid navigation method, combining trackless and magnetically tracked navigation, for an omnidirectional AMR (OAMR), in order to achieve trackless navigation in the absence of no magnetic tape paths, and switch to tracked navigation when a magnetic tape path is detected. For the trackless navigation, a dynamic motion controller is designed by integrating a backstepping PI kinematic control method and a fuzzy wavelet neural network (FWNN) augmented by a broad learning system (BLS), or abbreviated as FWNN-BLS. In the dynamic controller, the FWNN-BLS is employed to online learn uncertain dynamic behavior of the OAMR and then serve as a compensator, thus resulting in better performance and lower tracking errors during navigation. This dynamic controller works with the built Gmapping SLAM and A* global path algorithm to accomplish trackless navigation. For tracked navigation, the kinematic model of the OAMR is modified into a differential drive mode by setting the equal speeds of both wheels at the same side, and a PID controller is used with the magnetic guide sensor to carry out tracked navigation. The proposed hybrid navigation method is validated through simulations and experimental results, thus demonstrating its effectiveness and practicality.**

***Index Terms*—Dynamic control, fuzzy wavelet neural network-broad learning system (FWNN-BLS), hybrid navigation, omnidirectional AMR.**

I. Introduction

VARIOUS navigation strategies and control laws in the field of mobile robots have already been proposed by many researchers over many past years [1], in order to carry out desired navigation tasks according to navigation goals or missions. Generally speaking, the navigation tasks of mobile robots can be done by three navigation strategies: tracked, trackless and hybrid. Tracked navigation relies on external sensors for guided path tracking to implement navigation and cooperate with some control strategy to implement a stable path tracking approach; this navigation is normally used for automatic guide vehicles (AGVs) in industry. Trackless navigation means to employ simultaneous localization and mapping (SLAM) methods [2] and global and local path planning for autonomous navigation, and motion control strategies to track planned trajectories during navigation. Trackless navigation can be done by either model-based navigation by using four modules of motion control, perception, SLAM and recognition for path planning, or reactive paradigm [3], or using proper behaviors with respect to corresponding working environments [4]. Hybrid navigation strategy takes the advantages of tracked and trackless navigation according to physically operational requirements for AMRs. These three navigation strategies heavily rely upon the motion controllers and kinematic or dynamic models of mobile robots under consideration.

For trackless navigation, various algorithms have been proposed to plan desired navigation paths. In global path planning, algorithms such as A* [5] and RRT [6] were used for path planning. For local path planning, the dynamic window approach (DWA) [3] was often applied for obstacle avoidance. When executing path tracking, choosing the optimal control strategy is crucial. From PI control [7] to various modern intelligent control strategies, there have been a wide range of available methods. In terms of compensators, many intelligent control strategies, such as neural networks (NNs), fuzzy NNs and broad learning systems (BLSs) [8,9], can be used to optimally approximate the unknown functions or dynamics of the controller. The concept of BLSs can be proposed to expand the original two-layered neural network and optimize and improve parameter selection results under estimation by using more neurons [8,9], thus obtaining better control performance. In [10,11], FWNNs were utilized to achieve function or model approximations, or serve as compensator to improve control performance. However, there is still room for improvement in tracking error performance. This shortcoming motivates us to propose a novel model approximation method, dubbed as FWNN-BLS, by integrating fuzzy wavelet neural networks and broad learning systems, and investigate its application to serve as a compensator to compensate for the uncertainties caused by parameter variations of the OAMR.

In addition to the trackless navigation control methods based on the existing SLAMs, there is another type of navigation control scheme that relies on physical tracks. This type of navigation often depends on sensors and trajectory tracking control strategies. There are various types of sensors, such as magnetic guide sensors (Fig. 1(b)) and infrared reflective sensor [12], each of which is suited to different kinds of tracks. Note that these sensors come with their own precision issues. This paper plans to use an adjustable precision magnetic guide sensor along with magnetic tracks. In order to ensure effective navigation and accurate trajectory tracking, many control strategies and kinematic models have been proposed for the AMRs. This paper will attempt to use a magnetic guide sensor and modify the original OAMR kinematic model into a differential drive configuration. Further, the modified motion model will be combined with a PID controller strategy to establish a novel control method. This method not only matches the characteristics of the used sensors, but also achieves the goal of improving tracking control performance.

Manuscript received 24 September 2024; revised 17 October 2024; accepted 7 November; Date of publication 17 November 2024.

The authors deeply acknowledge financial support from the NSTC, Taiwan, ROC, under contract NSTC 112-2622- 8- 005 -005 -TE1.

Ching-Chih Tsai, Chi-Hsiang Li, Jia-Wei Su and Shih-Che Chen are with the Department of Electrical Engineering, National Chung Hsing University, Taichung, Taiwan, ROC. emails: cctsai@nchu.edu.tw, d107064201 @mail.nchu.edu.tw, g111064044 @mail.nchu.edu.tw, and d110064006 @mail.nchu.edu.tw, respectively.

Based on the studies in [8-12], this paper is targeted at proposing a hybrid navigation approach, which consists of trackless and tracked navigation. For trackless navigation, the

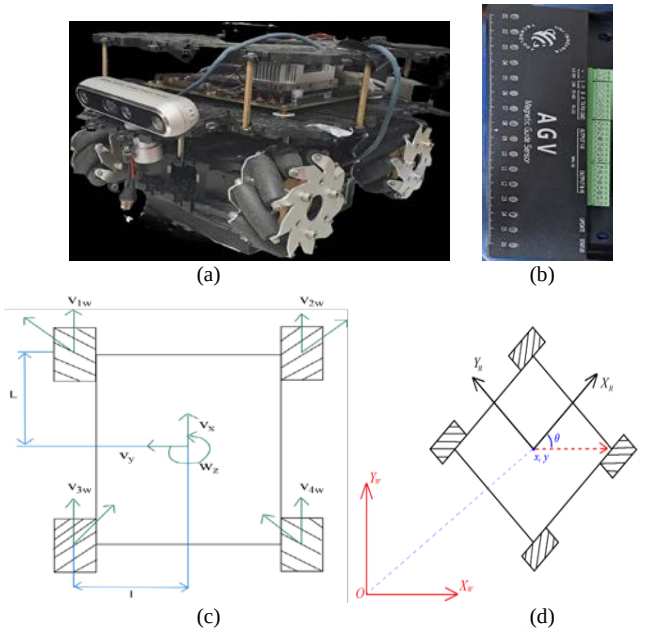

Fig. 1. The experimental OAMR. (a) Physical picture of the OAMR. (b) Picture of the used magnetic guide sensor. (c) Schematic diagram of the OAMR. (d) Robot pose definition in the world frame.

adopted scheme will integrate a FWNN-BLS compensator and a dynamic backstepping controller incorporating a dynamic model of the AMR and a kinematic PI controller. This new form of control strategy is proposed to achieve stable trajectory. In the part of tracked navigation, a new form of differential drive kinematics model together with a PID controller is investigated and applied in the OAMR. Through comparative simulations and experimental results, we will explore the advantages and merits of the control strategies for hybrid navigation.

The rest of the paper is structured as in the following sections. Section II introduces some preliminaries of the proposed method, including Kinematic PI control, navigation, and details of the navigation strategy outlined in the paper. It also introduces the FWNN-BLS neural network, the kinematic and dynamic models used for the OAMR, and the auxiliary application strategies for object detection. In Section III, the novel hybrid navigation control strategies are proposed in the navigation process, including the dynamic controller by combining the FWNN-BLS compensation and PI kinematic control, and the PID control for the tracked navigation is also constructed by using the differential-drive model on the omnidirectional AMR. Section IV analyzes the proposed method through simulation results. Experimental results shown in Section V demonstrate the effectiveness and applicability of the proposed method. Section VI concludes this paper.

II. Kinematic Control, Dynamic Model and some Preliminaries

The purpose of this section is to introduce the entire system architecture and some preliminaries of hybrid navigation, including the kinematic and dynamic model, as well as how object detection assists navigation applications. Additionally, this section will also introduce the concept of FWNN-BLS which can be used as a compensator design. Subsequent section will combine this neural network with PI controllers to form a novel compensation framework.

A. Kinematic PI Control

The robot platform used in this paper is a mobile robot equipped with four Mecanum wheels, as shown in Fig. 1(a). Here, the forward kinematics of the OAMR can be defined as in (1), which allows the conversion of the velocity command $\dot{\boldsymbol{X}}(t)=[\dot{x}(t)\ \dot{y}(t)\ \dot{\theta}(t)]^T$ into the motor speed commands denoted as $\boldsymbol{V}=\begin{bmatrix} v_{1w} & v_{2w} & v_{3w} & v_{4w}\end{bmatrix}^T$.

$$\boldsymbol{V}(t)=\boldsymbol{J}(\theta_1(t))\dot{\boldsymbol{X}}(t) \tag{1}$$

where $\boldsymbol{J}(\theta_1)=\begin{bmatrix}\sqrt{2}\sin(\theta_1) & -\sqrt{2}\cos(\theta_1) & -(l+L)\\ \sqrt{2}\cos(\theta_1) & \sqrt{2}\sin(\theta_1) & (l+L)\\ \sqrt{2}\cos(\theta_1) & \sqrt{2}\sin(\theta_1) & -(l+L)\\ \sqrt{2}\sin(\theta_1) & -\sqrt{2}\cos(\theta_1) & (l+L)\end{bmatrix}, \theta_1=\theta+\frac{\pi}{4}$

and $\boldsymbol{X}(t)=[x_w(t)\ y_w(t)\ \theta(t)]^T$ represents the pose of the OAMR and $l+L$ is a half of the sum of the length and width of the AMR, as depicted in Fig. 1(c) . Based on the kinematic model of the AMR, a PI controller is applied to achieve kinematic trajectory tracking for the OAMR. First, the tracking error, as defined in (2), is determined by calculating the difference between the mobile robot's position and the desired trajectory governed by $\boldsymbol{X}_r(t)=[x_r(t)\ y_r(t)\ \theta_r(t)]^T$.

$$\boldsymbol{X}_e(t)=\begin{bmatrix}x_e(t) & y_e(t) & \theta_e(t)\end{bmatrix}^T=\boldsymbol{X}(t)\text{-}\boldsymbol{X}_r(t) \tag{2}$$

Next, by utilizing the tracking error from (2), the kinematic model and PI controller can be integrated, where $\boldsymbol{K}_P$ and $\boldsymbol{K}_I$ are two symmetric and positive-definite matrices. This integration results in (3), enabling the robot to adjust its velocity in the world coordinate system through the PI controller. In Section III, this PI controller theory will be incorporated into the dynamic model to explore a more advanced and comprehensive control strategy.

$$\boldsymbol{V}(t)=\boldsymbol{J}(\theta_1(t))\cdot\left(-\boldsymbol{K}_p\boldsymbol{X}_e(t)-\boldsymbol{K}_I\left[\int_0^0\boldsymbol{X}_e(\tau)d\tau\right]+\dot{\boldsymbol{X}}_r(t)\right) \tag{3}$$

B. Dynamic Model

This subsection briefly recalls the dynamic model of the OAMR. The dynamic model allows for motion control through torque variations. Compared to the kinematic model, it considers more physical factors within the system, thereby providing better control for high-precision systems with faster motion speeds. Based on the dynamic model, its state equation is defined as in (4), which can be used to describe the entire system [13].

$$\dot{\boldsymbol{Y}}_1=\boldsymbol{Y}_2,\dot{\boldsymbol{Y}}_2=-\boldsymbol{f}+(R_\omega\boldsymbol{J}^+(\theta)\boldsymbol{M}^{-1})\boldsymbol{\tau} \tag{4}$$

where

$$\boldsymbol{J}^+(\theta_1)=\frac{1}{4}\begin{bmatrix}\sqrt{2}\sin(\theta_1) & \sqrt{2}\cos(\theta_1) & \sqrt{2}\cos(\theta_1) & \sqrt{2}\sin(\theta_1)\\ -\sqrt{2}\cos(\theta_1) & \sqrt{2}\sin(\theta_1) & \sqrt{2}\sin(\theta_1) & -\sqrt{2}\cos(\theta_1)\\ \frac{-1}{l+L} & \frac{1}{l+L} & \frac{-1}{l+L} & \frac{1}{l+L}\end{bmatrix}, \theta_1=\theta+\frac{\pi}{4}$$

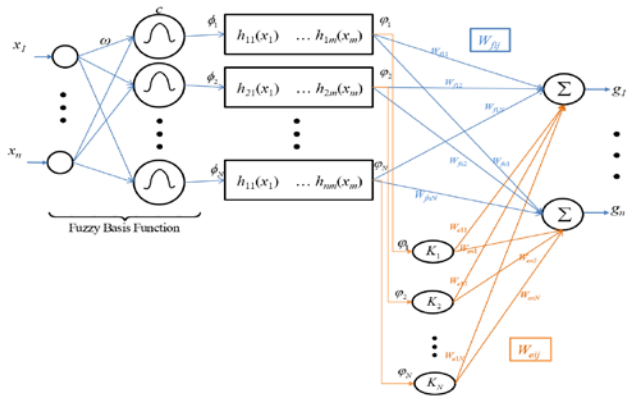

Fig. 2. Structure of the proposed FWNN-BLS.

Fig. 3. Experimental results of the object detection using YOLOv5.

Moreover, $\boldsymbol{Y_1}=[x_w \quad y_w \quad \theta]^T$ represents the pose of OAMR in the world coordinate system. The vector $\boldsymbol{f}$ is a compensation control quantity that will be approximated using the FWNN-BLS system introduced later. Parameter R_ω represents the radius of the wheels. Matrix $\boldsymbol{J}^+(\theta)$ represents the transformation matrix of OAMR, and matrix $\boldsymbol{M}$ represents the specific matrix constructed based on the robot's mass. The vector $\boldsymbol{\tau}$ represents the torque output of the robot's motors. For details of the dynamic model, please refer to [13].

C. FWNN-BLS

The subsection is aimed to describe the FWNN-BLS framework which combines fuzzy wavelet neural network (FWNN) and broad learning system (BLS). For detailed description of the BLS, the reader is referred to [8], where the BLS was proposed as a two-layer flat and feedforward neural network for which the first layer is with several mapped feature nodes, and the second layer is with many enhancement nodes, and all the outputs of the nodes in both layers are connected to the final output. Worthy of mention is that all the parameters of the BLS in [8] are found by using the well-known least-squares method. Fig. 2 shows the proposed FWNN-BLS structure, where the original FWNN architecture integrates fuzzy logic with wavelet analysis techniques, thus improving better function approximation and unknown model dynamics approximation, and optimizing numerical prediction. Note that h_{i1}, i=1,..,m, denotes the fuzzy wavelet function defined in [11]. The fuzzy logic can help process nonlinear related data or more complex applications with noise to help optimize the entire system. The FWNN can be integrated with the BLS system to enhance overall numerical prediction performance. Using the FWNN network as the primary framework, it is logically reasonable to integrate the BLS system to online learn the unknown dynamic model of the AMR, and then serve as a relevant compensator, thus achieving better high- performance OAMR tracking control.

D. Object Detection

This subsection briefly introduces the object detection method for object or place recognition [14]. In addition to the precise localization system and tracking control strategy required during the navigation process, additional tools can also be used to assist us in identifying places. Furthermore, the image recognition strategy is the mainstream to let the OAMR recognize some surrounding landmarks, in order to fuse multi-sensor readings to obtain better robot localization accuracy. In this paper, YOLOv5 model [15] is used to perform object or landmark detection work. It is expected to achieve the effect of assisting navigation by matching with iconic scenery or landmarks in the environment, allowing for better determination of the current location of the objects and landmarks as shown in Fig. 3. Overall, the measured landmark information using YOLOv5 model can be fused with the 2D LiDAR readings and odometry of the OAMR, thereby obtaining better robot localization [16].

E. Differential Drive Model

The purpose of this subsection is to introduce a new differential-drive kinematic model applied to the four-wheeled OAMR that achieves tracked navigation with the magnetic guide sensor. This model enables the robot itself to more conveniently control wheel movement. To do so, let us set $v_L = v_{1w} = v_{3w}$ and $v_R = v_{2w} = v_{4w}$ in (1) where v_L represents the speed of the two wheels on the left side of OAMR, and v_R represents the speed of the two wheels on the right side of OAMR. Thus, (1) turns out

$$\begin{bmatrix}\dot{x}_w\\ \dot{y}_w\\ \dot{\theta}\end{bmatrix}=\frac{1}{4}\begin{bmatrix}\sqrt{2}\sin(\theta_1)+\sqrt{2}\cos(\theta_1) & \sqrt{2}\sin(\theta_1)+\sqrt{2}\cos(\theta_1)\\ \sqrt{2}\sin(\theta_1)-\sqrt{2}\cos(\theta_1) & \sqrt{2}\sin(\theta_1)-\sqrt{2}\cos(\theta_1)\\ -\frac{2}{L+l} & \frac{2}{L+l}\end{bmatrix}\begin{bmatrix}v_L\\ v_R\end{bmatrix} \tag{5}$$
$$=\frac{1}{2}\begin{bmatrix}\cos(\theta) & \cos(\theta)\\ \sin(\theta) & \sin(\theta)\\ -\frac{1}{L+l} & \frac{1}{L+l}\end{bmatrix}\begin{bmatrix}v_L\\ v_R\end{bmatrix}=\begin{bmatrix}v_g\cos(\theta)\\ v_g\sin(\theta)\\ \omega_g\end{bmatrix}$$

where

$$v_g=(v_L+v_R)/2 \tag{6}$$

and

$$\omega_g=\frac{1}{2(L+l)}(v_R-v_L) \tag{7}$$

Note that the linear velocity, v_g, is expressed as the average of the left and right wheel speeds and the angular velocity, ω_g, is produced by the difference between speeds of the right and left wheels. As can be seen in (5), the forward kinematic model of the OAMR with the four Mecanum wheels is reduced to its differential drive forward kinematic one.

III. Proposed Hybrid Navigation

This section aims to present the hybrid navigation and its tracking control methods used in navigation. The first method is for tracked navigation, where the original OAMR kinematic model is modified into a two-wheeled differential mode

combined with a PID controller. This method not only

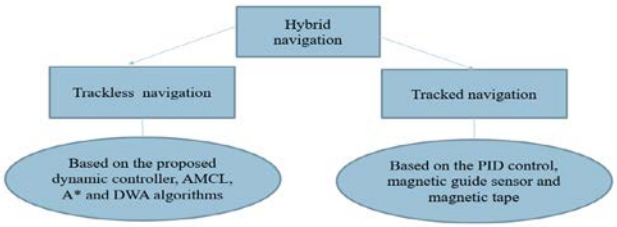

Fig. 4. Simple hierarchical structure of the proposed hybrid navigation.

enhances system stability but also provides a simpler method for motor control. The second method utilizes a novel control strategy that integrates a dynamic model of the OAMR, the backstepping PI control method, and FWNN-BLS for trackless navigation. This approach offers better performance compared to traditional FWNN compensators.

A. Hybrid Navigation

This subsection introduces the working principle of the hybrid navigation strategy. Fig. 4 depicts the simple hierarchical structure of the proposed hybrid navigation which is divided into two parts. The first part is to carry out trackless navigation on OAMR. Here, the trackless navigation first uses SLAM and applies the A* algorithm for global path planning from the starting point to the target point in the environment. After planning the global path, the paper considers the mobile robot performance in trajectory tracking. This section aims to propose a novel dynamic model control strategy to achieve path tracking and stable control. The second part of hybrid navigation uses tracked navigation and control, where the magnetic guide sensor will be used. This part uses the sensors and magnetic tape to track the path and implement an improved differential kinematic model based on the OAMR combined with a PID controller. Combining both strategies to achieve hybrid navigation goals will facilitate more efficient tracking control in navigation. In hybrid navigation, it is expected to first process trackless navigation to steer the AMR to reach a target point near a magnetic tape path, and then use the magnetic guide sensor in conjunction with a PID control and the magnetic tape path to proceed with tracked navigation.

In what follows the dynamic controller with the FWNN-BLS compensator is designed by the use of backstepping, where such dynamic motion controller is proposed to steer the OAMR to follow desired trajectories with appropriate actuation commands given by the PID path tracking controller in Section III.B or the kinematic controller in Section II.A. For such a backstepping controller design, an appropriate Lyapunov function is adopted to not only ensure the closed-loop stability of the AMR with the proposed dynamic controller, but also find the parameter adjustment rules of the FWNN-BLS compensator simultaneously. These parameter updating rules are then employed to renew all the parameters of the FWNN-BLS compensator, in order to guarantee the closed-loop stability of the overall control system.

B. PID Control for Tracked Navigation

In magnetically guided tracked navigation, the PID control strategy is employed to adjust the mobile robot's angular velocity, indirectly regulating the wheel speeds. This enables the robot to accurately track along the magnetic tape path. Below is a more comprehensive detail of the controller. First, define the PID controller as shown in (8), which can utilize the central deviation measured by the magnetic guide sensor to correct the angular velocity ω_g of the OAMR through the controller, where K_P, K_I and K_D are the three-term parameters of the controller. By combining (7) and (8), the rearranged result of (9) can be obtained.

$$\omega_g = \tfrac{1}{2(L+l)}(v_R - v_L) = K_P e(t) + K_I \int_0^t e(\tau)d\tau + K_D \frac{de(t)}{dt} \tag{8}$$

where

$$v_R - v_L = 2(L+l)\omega_g, v_L + v_R = 2v_g \tag{9}$$

Finally, based on the set speed v_g and ω_g adjusted by the PID controller, the speeds, v_L and v_R, of the left and right wheels can be obtained by (10), respectively.

$$v_R = v_g + (L+l)\omega_g, v_L = v_g - (L+l)\omega_g \tag{10}$$

Next, let us move to discuss the stability of the controller. In doing so, we first assume that the PID controller operates well. Thus, it is easy to find the closed-loop transfer function as in (12). Once the PID gains, K_P, K_I and K_D, have been chosen to stabilize the system in (13), it easily shows that the tracking errors tend to zero as shown in (14). In doing so, one uses the Laplace transform to obtain from (8)

$$\omega_g(s) = (K_p + K_I \frac{1}{s} + K_D s)E(s), \theta(s) = \frac{1}{s}\omega_g(s) \tag{11}$$

which leads to the closed-loop transfer function $T(s)$ as

$$T(s) = \frac{\theta(s)}{\theta_r(s)} = \frac{K_D s^2 + K_P s + K_I}{(1+K_D)s^2 + K_P s + K_I} \tag{12}$$

where $\theta_r(s)$ means the desired robot heading. Next, let its characteristic equation be stabilized by

$$(1+K_D)s^2 + K_P s + K_I = 0 \tag{13}$$

such that the tracking error approaches zero if $\theta_r(s)$ is a step command, i.e.,

$$e(t) = \theta_r(t) - \theta(t) \to 0, \text{ as } t \to \infty. \tag{14}$$

Worthy of mention is that, if K_D is set by zero, then the PI controller can be used to accomplish path tracking if appropriate K_P and K_I gains are real and positive.

C. Dynamic Control Using FWNN-BLS

In trackless navigation based on the state equation (4) of the OAMR's dynamic model from Section II, this subsection focuses on the proposed novel dynamic control strategy with the FWNN-BLS compensator. First, the tracking error vector (15) is defined, where $\boldsymbol{Y_r} = [x_r \ y_r \ \theta_r]^T$ represents the position state vector of the tracking reference.

$$\boldsymbol{Y_{1e}} = \boldsymbol{Y_1} - \boldsymbol{Y_r}, \boldsymbol{Y_{2e}} = \dot{\boldsymbol{Y}}_1 - \dot{\boldsymbol{Y}}_r \tag{15}$$

The PI control used in the kinematic model can be imported into the dynamic model, and the time differential results of (15) can be rewritten into (16) and (17).

$$\dot{\boldsymbol{Y}}_{1e} = \dot{\boldsymbol{Y}}_1 - \dot{\boldsymbol{Y}}_r = -\boldsymbol{K}_p \boldsymbol{Y}_{1e} - \boldsymbol{K}_I \int \boldsymbol{Y}_{1e}(\tau) d\tau \tag{16}$$

$$\dot{\boldsymbol{Y}}_{2e} = \ddot{\boldsymbol{Y}}_1 - \ddot{\boldsymbol{Y}}_r = -\boldsymbol{f} + (R_\omega \boldsymbol{J}^+(\theta)\boldsymbol{M}^{-1})\boldsymbol{\tau} - \ddot{\boldsymbol{Y}}_r \tag{17}$$

The Lyapunov function V_1 is selected as in (18) in this part.

$$V_1 = \frac{1}{2}\boldsymbol{Y}_{1e}{}^T \boldsymbol{Y}_{1e} + \frac{1}{2}\int \boldsymbol{Y}_{1e}{}^T(\tau)\boldsymbol{K}_I \boldsymbol{Y}_{1e}(\tau) d\tau \tag{18}$$

By introducing the results of (15) and (16) into (18), the result of (19) can be obtained by differentiating V_1 with respect to time, thus leading to find

$$\begin{aligned} \dot{V}_1 &= \boldsymbol{Y}_{1e}{}^T \dot{\boldsymbol{Y}}_{1e} + \int \boldsymbol{Y}_{1e}{}^T(\tau) d\tau \boldsymbol{K}_I \boldsymbol{Y}_{1e}(t) = \boldsymbol{Y}_{1e}{}^T(-\boldsymbol{K}_p \boldsymbol{Y}_{1e} \\ &-\boldsymbol{K}_I \int \boldsymbol{Y}_{1e}(\tau) d\tau) + \int \boldsymbol{Y}_{1e}{}^T(\tau) d\tau)^T \boldsymbol{K}_I \boldsymbol{Y}_{1e} = -\boldsymbol{Y}_{1e}{}^T \boldsymbol{K}_p \boldsymbol{Y}_{1e} \le 0 \end{aligned} \tag{19}$$

Barbalat's lemma and LaSalle's theorem imply that $\boldsymbol{Y}_{1e} \to 0$ as $t \to \infty$. Furthermore, since $\boldsymbol{Y}_{1e} \equiv \boldsymbol{0}$ and $\boldsymbol{K}_I$ is symmetric and positive-definite, then we have

$$\dot{\boldsymbol{Y}}_{1e} \equiv \boldsymbol{0} = -(\boldsymbol{K}_P \underbrace{\boldsymbol{Y}_{1e}}_{0} + \boldsymbol{K}_I \int \boldsymbol{Y}_{1e}(\tau) d\tau) \Rightarrow \boldsymbol{K}_I \int \boldsymbol{Y}_{1e}(\tau) d\tau \equiv \boldsymbol{0} \Rightarrow \int \boldsymbol{Y}_{1e}(\tau) d\tau \equiv \boldsymbol{K}_I{}^{-1} \boldsymbol{0} = \boldsymbol{0}.$$

Continuing from the backstepping control, the method introduces the concept of virtual control and defines backstepping error $\boldsymbol{\xi}$ as shown by (20)

$$\boldsymbol{\xi} = \boldsymbol{Y}_2 - \phi(\boldsymbol{Y}_{1e}) = \boldsymbol{Y}_{2e} + \boldsymbol{K}_P \boldsymbol{Y}_{1e} + \boldsymbol{K}_I \int \boldsymbol{Y}_{1e}(\tau) d\tau \tag{20}$$

With the backstepping control, $\dot{\boldsymbol{Y}}_{1e}$ can be rewritten as

$$\dot{\boldsymbol{Y}}_{1e} = \boldsymbol{Y}_{2e} = \boldsymbol{\xi} - (\boldsymbol{K}_P \boldsymbol{Y}_{1e} + \boldsymbol{K}_I \int \boldsymbol{Y}_{1e}(\tau) d\tau) \tag{21}$$

Moreover, the time differentiation of backstepping error $\boldsymbol{\xi}$ can be found as in (22)

$$\dot{\boldsymbol{\xi}} = -\boldsymbol{f} + (r\boldsymbol{J}^+(\boldsymbol{\theta})\boldsymbol{M}_0{}^{-1})\boldsymbol{\tau} - \ddot{\boldsymbol{Y}}_r + \boldsymbol{K}_P \dot{\boldsymbol{Y}}_{1e} + \boldsymbol{K}_I \boldsymbol{Y}_{1e} \tag{22}$$

The following control law is proposed to stabilize the dynamic model of the backstepping error.

$$\begin{aligned} \boldsymbol{\tau} &= \frac{1}{r}\boldsymbol{M}_0 \boldsymbol{J}(\theta)[\boldsymbol{f} + \ddot{\boldsymbol{Y}}_r - \boldsymbol{K}_P \dot{\boldsymbol{Y}}_{1e} - \boldsymbol{K}_I \boldsymbol{Y}_{1e} - \boldsymbol{K}_I \boldsymbol{\xi} - \boldsymbol{Y}_{1e}] \\ &= \frac{1}{r}\boldsymbol{M}_0 \boldsymbol{J}(\theta)[\boldsymbol{f} + \ddot{\boldsymbol{Y}}_r - \boldsymbol{K}_p(\boldsymbol{\xi} - \boldsymbol{K}_P \boldsymbol{Y}_{1e} - \boldsymbol{K}_I \int \boldsymbol{Y}_{1e}(\tau) d\tau) - \boldsymbol{K}_I \boldsymbol{Y}_{1e} - \boldsymbol{Y}_{1e} - \boldsymbol{K}_I \boldsymbol{\xi}] \end{aligned} \tag{23}$$

Equation (24) shows the chosen Lyapunov function planned in this stability analysis.

$$V_2 = V_1 + (\boldsymbol{\xi}^T \boldsymbol{\xi})/2 \tag{24}$$

By taking the results of (20) and (21), the time derivative of (24) can be obtained. The use of LaSalle's theorem yields that $\boldsymbol{Y}_{1e} \to 0$ and $\boldsymbol{\xi} \to 0$ as $t \to \infty$.

$$\begin{aligned} \dot{V}_2 &= \dot{V}_1 + \boldsymbol{\xi}^T \dot{\boldsymbol{\xi}} = \dot{V}_1 + \boldsymbol{\xi}^T(-\boldsymbol{K}_I \boldsymbol{\xi} - \boldsymbol{Y}_{1e}) = \\ &= \boldsymbol{Y}_{1e}{}^T(\boldsymbol{\xi} - (\boldsymbol{K}_P \boldsymbol{Y}_{1e} + \boldsymbol{K}_I \int \boldsymbol{Y}_{1e}(\tau) d\tau)) + (\int \boldsymbol{Y}_{1e}(\tau) d\tau)^T \boldsymbol{K}_I \boldsymbol{Y}_{1e}(\tau)) \\ &+ \boldsymbol{\xi}^T(-\boldsymbol{K}_I \boldsymbol{\xi} - \boldsymbol{Y}_{1e}) = \underbrace{-\boldsymbol{\xi}^T \boldsymbol{K}_I \boldsymbol{\xi}}_{<0} \underbrace{-\boldsymbol{Y}_{1e}{}^T \boldsymbol{K}_P \boldsymbol{Y}_{1e}}_{<0} \le 0 \end{aligned} \tag{25}$$

Furthermore, it turns out

$$\begin{aligned} &\dot{\boldsymbol{Y}}_{1e} \equiv 0 = -(\boldsymbol{K}_P \underbrace{\boldsymbol{Y}_{1e}}_{0} + \boldsymbol{K}_I \int \boldsymbol{Y}_{1e}(\tau) d\tau) + \underbrace{\boldsymbol{\xi}}_{0} \Rightarrow \boldsymbol{K}_I \int \boldsymbol{Y}_{1e}(\tau) d\tau \equiv 0 \\ &\Rightarrow \int \boldsymbol{Y}_{1e}(\tau) d\tau \equiv \boldsymbol{K}_I{}^{-1} 0 = 0. \end{aligned}$$

Next, move to discuss the FWNN-BLS compensation. The FWNN-BLS will be first utilized to online approximate the unknown vector $\boldsymbol{f}$. Based on an FWNN as the main architecture and then combined with the BLS, this FWNN-BLS is mainly applied to achieve a better approximation result for the unknown vector $\boldsymbol{f}$. The following description will explain the concept and algorithm of its operation in more detail. The unknown vector $\boldsymbol{f}$ can be well approximated by the neural network using (26), where $\boldsymbol{W}_{fi}$ is the weight vector of the FWNN, $\boldsymbol{W}_{ei}$ is the weight vector of the BLS, $\boldsymbol{K}(\boldsymbol{\varphi})$ is the regression vector of the enhancement nodes in the BLS, and finally $\boldsymbol{W}_i$ is the overall weight vector of the FWNN-BLS.

$$\boldsymbol{f}_i = \boldsymbol{W}_{ei}{}^T \boldsymbol{K}(\boldsymbol{\varphi}) + \boldsymbol{W}_{fi}{}^T \varphi(\boldsymbol{x}, \hat{\boldsymbol{c}}, \hat{\boldsymbol{\omega}}) = \boldsymbol{W}_i^T \boldsymbol{\Phi}(\boldsymbol{x}, \hat{\boldsymbol{c}}, \hat{\boldsymbol{\omega}}) \tag{26}$$

Define the relevant parameters as follows, $\tilde{\boldsymbol{\omega}} = \boldsymbol{\omega}^* - \hat{\boldsymbol{\omega}}$, $\tilde{\boldsymbol{\varphi}} = \boldsymbol{\varphi}^* - \hat{\boldsymbol{\varphi}}$, $\tilde{\boldsymbol{W}} = \boldsymbol{W}^* - \hat{\boldsymbol{W}}$. Then (26) is rewritten to form (27)

$$\begin{aligned} \boldsymbol{f} &= \boldsymbol{W}^{*T} \boldsymbol{\Phi}^*(\boldsymbol{x}, \boldsymbol{c}^*, \boldsymbol{\omega}^*) + \boldsymbol{\varepsilon}_f^* = (\tilde{\boldsymbol{W}} + \hat{\boldsymbol{W}})^T (\tilde{\boldsymbol{\Phi}} + \hat{\boldsymbol{\Phi}}) + \boldsymbol{\varepsilon}_f^* \\ &= \hat{\boldsymbol{f}} + \hat{\boldsymbol{W}}^T \tilde{\boldsymbol{\Phi}} + \tilde{\boldsymbol{W}}^T \hat{\boldsymbol{\Phi}} + \tilde{\boldsymbol{W}}^T \tilde{\boldsymbol{\Phi}} + \boldsymbol{\varepsilon}_f^* \end{aligned} \tag{27}$$

Based on the Taylor series expansion, $\tilde{\boldsymbol{\Phi}}$ can be calculated by (28) to obtain the result.

$$\tilde{\boldsymbol{\Phi}} = \frac{\partial \tilde{\boldsymbol{\Phi}}}{\partial \hat{\boldsymbol{\omega}}} \tilde{\boldsymbol{\omega}} + \frac{\partial \tilde{\boldsymbol{\Phi}}}{\partial \hat{\boldsymbol{\omega}}} \tilde{\boldsymbol{\omega}} + \boldsymbol{H} = \boldsymbol{A}\tilde{\boldsymbol{\omega}} + \boldsymbol{B}\tilde{\boldsymbol{c}} + \boldsymbol{H} \tag{28}$$

Continuing the result $\tilde{\boldsymbol{\Phi}}$ obtained from (28), which can be rewritten as (29), then $\boldsymbol{h} = \hat{\boldsymbol{W}}^T \boldsymbol{H} + \boldsymbol{\varepsilon}$ can be defined, and the compensation vector $\boldsymbol{f}$ can be rewritten as the result of (30).

$$\boldsymbol{f} = \hat{\boldsymbol{f}} + \hat{\boldsymbol{W}}^T \boldsymbol{A}\tilde{\boldsymbol{\omega}} + \hat{\boldsymbol{W}}^T \boldsymbol{B}\tilde{\boldsymbol{c}} + \tilde{\boldsymbol{W}}^T \hat{\boldsymbol{\Phi}} + \hat{\boldsymbol{W}}^T \boldsymbol{H} + \boldsymbol{\varepsilon} \tag{29}$$

$$\boldsymbol{f} = \hat{\boldsymbol{f}} + \hat{\boldsymbol{W}}^T \boldsymbol{A}\tilde{\boldsymbol{\omega}} + \hat{\boldsymbol{W}}^T \boldsymbol{B}\tilde{\boldsymbol{c}} + \tilde{\boldsymbol{W}}^T \hat{\boldsymbol{\Phi}} + \boldsymbol{h} \tag{30}$$

With the FWNN-BLS, the approximate result of $\boldsymbol{f}$, the vector $\boldsymbol{\tau}$ in the dynamic model is proposed as in (31), where $K_3 \in R > \|h\|_\infty$, and r is the wheel radius.

$$\boldsymbol{\tau} = \frac{1}{r}\boldsymbol{M}\boldsymbol{J}(\theta)\begin{bmatrix} \hat{\boldsymbol{f}} + \ddot{\boldsymbol{Y}}_r - \boldsymbol{K}_P(\boldsymbol{\xi} - \boldsymbol{K}_P \boldsymbol{Y}_{1e} - \boldsymbol{K}_I \int \boldsymbol{Y}_{1e}(\tau) d\tau) - \\ \boldsymbol{K}_I \boldsymbol{Y}_{1e} - \boldsymbol{K}_I \boldsymbol{\xi} - \boldsymbol{Y}_{1e} - K_3 \boldsymbol{sgn}(\boldsymbol{\xi}) \end{bmatrix} \tag{31}$$

With the approximate result of $\boldsymbol{f}$, then $\dot{\boldsymbol{\xi}}$ turns out

$$\begin{aligned}\dot{\xi} &= -\boldsymbol{f} + \boldsymbol{K}_P(\xi - (\boldsymbol{K}_P\boldsymbol{Y}_{1e} + \boldsymbol{K}_I\int \boldsymbol{Y}_{1e}(\tau)d\tau)) + \boldsymbol{K}_I\boldsymbol{Y}_{1e} - \ddot{\boldsymbol{Y}}_r \\ &+ r\boldsymbol{J}^+(\theta)\boldsymbol{M}^{-1}\frac{1}{r}\boldsymbol{M}\boldsymbol{J}(\theta)\Big[\hat{\boldsymbol{f}} + \ddot{\boldsymbol{Y}}_r - \boldsymbol{K}_P(\xi - \boldsymbol{K}_P\boldsymbol{Y}_{1e} - \boldsymbol{K}_I\int \boldsymbol{Y}_{1e}(\tau)d\tau)\Big] \\ &+ r\boldsymbol{J}^+(\theta)\boldsymbol{M}^{-1}\frac{1}{r}\boldsymbol{M}\boldsymbol{J}(\theta)\big[-\boldsymbol{K}_I\boldsymbol{Y}_{1e} - \boldsymbol{K}_I\xi - \boldsymbol{Y}_{1e} - K_3\boldsymbol{sgn}(\xi)\big] \\ &= -\hat{\boldsymbol{W}}^T\boldsymbol{A}\tilde{\omega} - \hat{\boldsymbol{W}}^T\boldsymbol{B}\tilde{c} - \tilde{\boldsymbol{W}}^T\hat{\varphi} - \boldsymbol{h} - \boldsymbol{K}_I\xi - \boldsymbol{Y}_{1e} - K_3\boldsymbol{sgn}(\xi)\end{aligned} \tag{32}$$

The result of $\xi^T\xi$ can be subsequently imported into the Lyapunov function to prove the stability of the system.

$$\begin{aligned}\xi^T\dot{\xi} &= -\xi^T\hat{\boldsymbol{W}}^T\boldsymbol{A}\tilde{\omega} - \xi^T\hat{\boldsymbol{W}}^T\boldsymbol{B}\tilde{c} - \xi^T\tilde{\boldsymbol{W}}^T\hat{\boldsymbol{j}} - \xi^T\boldsymbol{h} - \xi^T\boldsymbol{K}_I\xi \\ &- \xi^T\boldsymbol{Y}_{1e} - K_3\xi^T\,\mathrm{sgn}(\xi) \le -\xi^T\hat{\boldsymbol{W}}^T\boldsymbol{A}\tilde{\omega} - \xi^T\hat{\boldsymbol{W}}^T\boldsymbol{B}\tilde{c} - \xi^T\tilde{\boldsymbol{W}}^T\hat{\boldsymbol{j}} \\ &- \xi^T\boldsymbol{K}_I\xi - \xi^T\boldsymbol{Y}_{1e} + \left(\|h\|_\infty - K_3\right)\|\xi\|_1\end{aligned} \tag{33}$$

In order to prove the stability of the entire system, the Lyapunov function V_3 is selected as in (34),

$$V_3 = V_2 + tr\left[\tilde{\boldsymbol{W}}^T\boldsymbol{K}_w^{-1}\tilde{\boldsymbol{W}}\right] + tr\left[\tilde{\boldsymbol{c}}^T\boldsymbol{K}_c^{-1}\tilde{\boldsymbol{c}}\right] + tr\left[\tilde{\boldsymbol{\omega}}^T\boldsymbol{K}_\omega^{-1}\tilde{\boldsymbol{\omega}}\right] \tag{34}$$

where K_w, K_c and K_ω are the matrices with appropriate dimensions.

$$\begin{aligned}\dot{V}_3 &= \boldsymbol{Y}_{1e}^T\dot{\boldsymbol{Y}}_{1e} + (\int \boldsymbol{Y}_{1e}(\tau)d\tau)^T\boldsymbol{K}_I\boldsymbol{Y}_{1e}(\tau)) + \xi^T\dot{\xi} \\ &+ \boldsymbol{tr}\left[-\tilde{\boldsymbol{W}}^T\boldsymbol{K}_w^{-1}\dot{\hat{\boldsymbol{W}}}\right] + \boldsymbol{tr}\left[-\tilde{\boldsymbol{c}}^T\boldsymbol{K}_c^{-1}\dot{\hat{\boldsymbol{c}}}\right] + \boldsymbol{tr}\left[-\tilde{\boldsymbol{\omega}}^T\boldsymbol{K}_\omega^{-1}\dot{\hat{\boldsymbol{\omega}}}\right] \\ &= \boldsymbol{Y}_{1e}^T(\xi - \boldsymbol{K}_P\boldsymbol{Y}_{1e} - \boldsymbol{K}_I\int \boldsymbol{Y}_{1e}(\tau)d\tau) + (\int \boldsymbol{Y}_{1e}(\tau)d\tau)^T\boldsymbol{K}_I\boldsymbol{Y}_{1e}(\tau)) + \\ &(-\xi^T\hat{\boldsymbol{W}}^T\boldsymbol{A}\tilde{\omega} - \xi^T\hat{\boldsymbol{W}}^T\boldsymbol{B}\tilde{c} - \xi^T\tilde{\boldsymbol{W}}^T\hat{\boldsymbol{j}} - \xi^T\boldsymbol{K}_I\xi - \xi^T\boldsymbol{Y}_{1e} - \left(K_3 - \|h\|_\infty\right)\|\xi\|_1) \\ &- tr\left[\tilde{\boldsymbol{W}}^T\boldsymbol{K}_w^{-1}\dot{\hat{\boldsymbol{W}}} + \tilde{\boldsymbol{W}}^T\hat{\boldsymbol{\Phi}}\xi^T\right] - tr\left[\tilde{\boldsymbol{c}}^T\boldsymbol{K}_c^{-1}\dot{\hat{\boldsymbol{c}}} + \tilde{\boldsymbol{c}}^T\boldsymbol{B}^T\hat{\boldsymbol{W}}\xi\right] - tr\left[\tilde{\boldsymbol{\omega}}^T\boldsymbol{K}_\omega^{-1}\dot{\hat{\boldsymbol{\omega}}} + \tilde{\boldsymbol{\omega}}^T\boldsymbol{A}^T\hat{\boldsymbol{W}}\xi\right]\end{aligned} \tag{35}$$

In order to prove system stability, one sets

$-tr\left[\tilde{c}^T(k_c^{-1}\dot{\hat{\boldsymbol{c}}} + \boldsymbol{B}^T\hat{\boldsymbol{W}}\xi)\right] = 0$, $-tr\left[\tilde{\boldsymbol{\omega}}^T(\mathrm{k}_\mathrm{w}^{-1}\dot{\hat{\boldsymbol{\omega}}} + \boldsymbol{A}^T\hat{\boldsymbol{W}}\xi)\right] = 0$, and $-tr\left[\tilde{\boldsymbol{W}}^T(k_\omega^{-1}\dot{\hat{\boldsymbol{W}}} + \xi\hat{\varphi}^T)\right] = 0$ in $\dot{V}_3$. Here, we have

$$\dot{V}_3 \le -\boldsymbol{Y}_{1e}^T\boldsymbol{K}_P\boldsymbol{Y}_{1e} - \xi^T\boldsymbol{K}_I\xi - \left(K_3 - \|h\|_\infty\right)\|\xi\|_1) \le 0 \text{ if } K_3 > \|h\|_\infty \tag{36}$$

The use of LaSalle invariance theorem implies that $\boldsymbol{Y}_{1e} \to 0$ and $\xi \to 0$ as $t \to \infty$. The system is eventually shown uniformly asymptotically stable. Based on the aforementioned stability proof process, it can lead to the underlying parameter adjustment rules for the FWNN-BLS.

$$\dot{\hat{c}} = -k_c\boldsymbol{B}^T\hat{\boldsymbol{W}}\xi,\ \ \dot{\hat{\omega}} = -k_\omega\boldsymbol{A}^T\hat{\boldsymbol{W}}\xi,\ \ \dot{\hat{\boldsymbol{W}}} = -k_w\hat{\boldsymbol{\varphi}}\xi^T \tag{37}$$

IV. Simulations and Discussion

This section will conduct three simulations to examine the effectiveness of the proposed tracked navigation, dynamic control method and trackless navigation method. During the three simulations, the weight of the OAMR is 4 kg, the body length and width are set by *L*=22 cm and *l*=20 cm, respectively, and the wheel radius is *r*=5 cm. Moreover, Matlab programs are written to study the effectiveness and performance of the three proposed methods.

A. Tracked Navigation

In this subsection, the first simulation is done to verify the efficacy of the proposed tracked navigation method, which involves a two-wheeled differential-drive model combined with PID controller in the tracked navigation of the OAMR. The PID parameters, as computed in (38), by matching the second-order characteristic equation, $s^2 + 2\xi\omega_n s + \omega_n^2 = 0$,

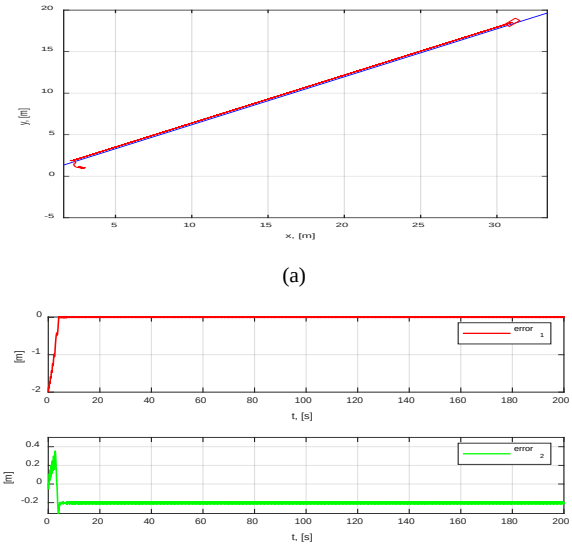

(a)

(b)

Fig. 5. Tracked Navigation. (a) Tracking result of the magnetic guide tracking where the starting point was put at the position of (0.9m,2.0m). (b) Tracking errors in the x and y frames, respectively.

are determined through selecting ζ and planning the settling time and frequency response ω . This rule indirectly calculates the gains of K_P, K_I, and K_D.

$$K_I/(1+K_D) = \omega^2, K_P/(1+K_D) = 2\xi\omega \tag{38}$$

Therefore, the controller parameters are set by selecting K_D as 0.6, K_P, as 2.5, and K_I as 0.9, respectively. Fig. 5(a) shows the effectiveness of path tracking using the PID controller, and Fig. 5(b) respectively illustrates the tracking errors in the *x* and *y* frames. The convergence of tracking errors on the x-axis and y-axis, as well as its stable performance, can be observed and confirmed in Fig.5, thus verifying the effectiveness of implementing the PID controller in the differential-drive model of the OAMR.

B. Proposed Dynamic Controller

The second simulation compares the circular trajectory tracking results of the proposed dynamic controller with the FWNN-BLS compensator and the traditional FWNN compensator in trackless navigation. In the FWNN-BLS controller parameter settings, the damping ratio is set to one, and the controller parameters $\boldsymbol{K}_p$ is set by $30*\boldsymbol{I}_2$ and $\boldsymbol{K}_I$ is tuned to $16*\boldsymbol{I}_2$. The simulation results presented in Fig. 5 show the circular trajectory tracking results for both compensators, and Fig. 6 shows the time evolutions of the tracking errors for both compensators. It can be concluded that the result of the FWNN-BLS compensator in Fig. 6(b) and Fig. 7(b) demonstrates better tracking and error convergence performance compared to the result of the FWNN

compensators in Fig. 6(a) and Fig. 7(a). This simulation further discusses the impact of settling time on trajectory tracking. As can be seen in Fig. 8, the result in Fig. 8(a) has a shorter settling time of 0.5 seconds and smaller tracking errors by comparing to the results in Fig. 8(b) which has a longer settling time of one second. Finally, the performance analyses of the dynamic controller with the FWNN and FWNN-BLS compensators are evaluated using the control performance indexes such as IAE

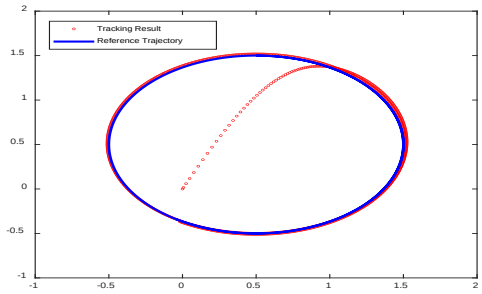

(a)

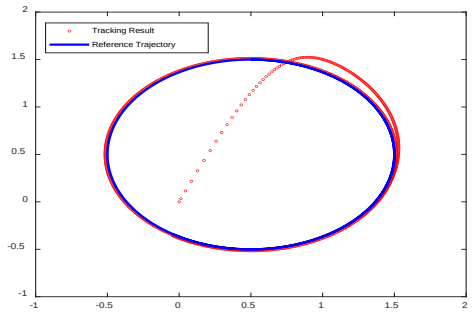

(b)

Fig. 6. Trajectory tracking simulation of the proposed dynamic controller where the starting point was put at the origin. (a) The simulation result of the controller with the FWNN compensator. (b) The simulation result of the controller with the FWNN-BLS compensator.

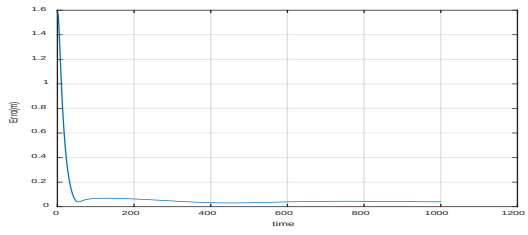

(a)

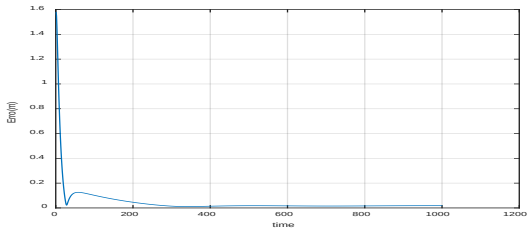

(b)

Fig. 7. Time evolutions of the trajectory tracking errors of the proposed dynamic controller the starting point was put at the origin. (a) The error plot of using the FWNN compensator. (b) The error plot of using the FWNN-BLS compensator.

TABLE I

PERFORMANCE COMPARISON OF THE PROPOSED DYNAMIC CONTROLLER WITH FWNN AND FWNN-BLS IN TERMS OF IAE AND ITAE (UNIT: M).

	IAE X	IAE Y	ITAE X	ITAE Y
FWNN	**0.1922**	**0.3572**	**0.5725**	**0.6259**
FWNN-BLS	**0.07759**	**0.1996**	**0.08543**	**0.1222**

and ITAE in Table I. The comparative results indicate that the proposed dynamic controller with the FWNN-BLS compensator demonstrates better tracking control performance than that with the FWNN compensator does.

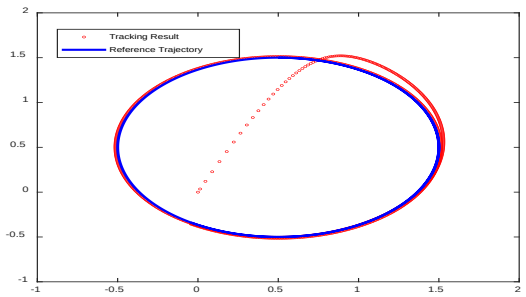

(a)

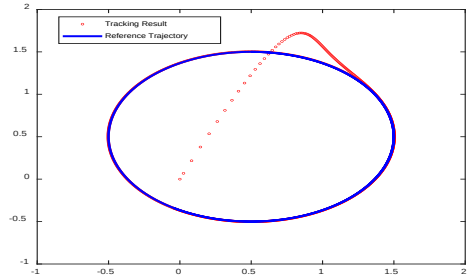

(b)

Fig. 8. Trajectory tracking of the second simulation where the starting point was set at the origin. (a) The tracking result of using the FWN-BLS with the settling time of 0.5 sec. (b) The tracking result of using the FWNN-BLS with the settling time of 1 sec.

C. Trackless Navigation

This subsection aims to carry out the third simulation to show the effectiveness of the proposed trackless navigation. During the simulation, the known Gmapping SLAM is utilized to build a map for the simulation environment as in Fig. 9(a). Once the environment map has been obtained, then A* algorithm is used for global path planning and the AMCL will be adopted for robot localization based on the built map. Furthermore, the previous dynamic controller is employed to track desired planned trajectories. Regarding parameter selection for the PI controller in (16) in trackless navigation simulation, the damping ratio is set by one, the settling time is set about 4.2 seconds. The proportional gain K_P is then computed as 1.9, while the integral gain K_I is found by 0.9. Gazebo and Rviz are employed to present the simulation results of trackless navigation. Fig. 9(b) illustrates the navigation results using Rviz, showing that the OAMR successfully follows the trajectory and completes the mission to reach the target point. Through the results in Fig. 9, the proposed trackless navigation using the proposed dynamic controller has

been shown effective in steering the OAMR to achieve trackless navigation.

V. Experimental Results and Discussion

In this section, three experiments are conducted to examine the control performance and applicability of tracked and trackless navigation methods for the OAMR. The first experiment uses the magnetic guide sensor and magnetic tape to practice tracked navigation based on the differential drive model of the AMR combined with the PID controller. The first

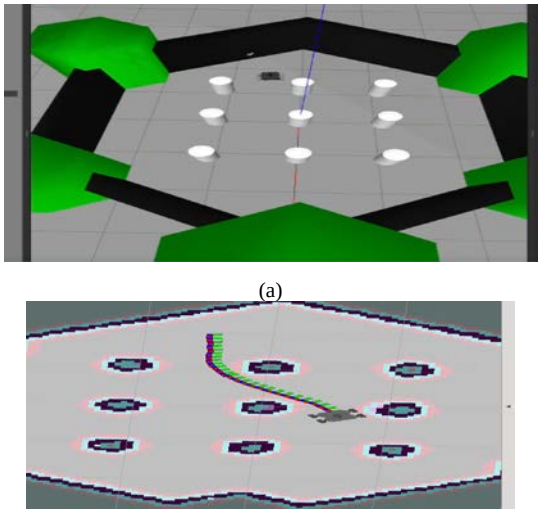

(a)

(a)

Fig. 9. Simulation of the trackless navigation. (a) Simulation environment using Gazebo. (b) Trackless navigation shown using Rviz.

(a) (b) (c)

Fig. 10. Still experimental pictures of tracked navigation from the beginning to the destination. (a) to (c) Robot movements from its beginning to destination during the tracked navigation.

experiment verifies the experimental results of the proposed dynamic controller. The first experiment presents the test results of trackless navigation with Gmapping SLAM and the dynamic controller incorporated with the FWNN-BLS compensator.

A. Experimental Results on Tracked Navigation

In the first experiment, let the damping ratio be set as unity, the settling time be about 5.7 seconds, and choose the derivative gain K_D as 0.5. Therefore, from (38), the proportional gain K_P was calculated by 2.5, and K_I was computed as 0.75. Fig. 10 depicts the experimental results of the tracked navigation with the PID path tracking controller. starting position. In the three still pictures from Fig.10 (a)-(c), the robot in Fig. 10(a) didn't enter the range of the magnetic tape, and then the robot began to gradually enter the sensing range and reached a tracking state after a period of transient response to follow the center of the tape in Fig.10 (b). After a turning point in Fig.10(c), the robot continued to track the center of the tape path stably, thus demonstrating the efficacy of the PID path tracking controller for tracked navigation. The experimental results indicate the practicability of this tracked navigation using the PID control strategy. Note that the renowned AMCL for localization can be used for robot localization during the tracked navigation.

B. Experiment on the Proposed Dynamic Controller

This subsection carries out the second experiment to verify the performance of the proposed dynamic controller. The parameter settings of the proposed dynamic controller were identical to those in the simulation case. The designed OAMR

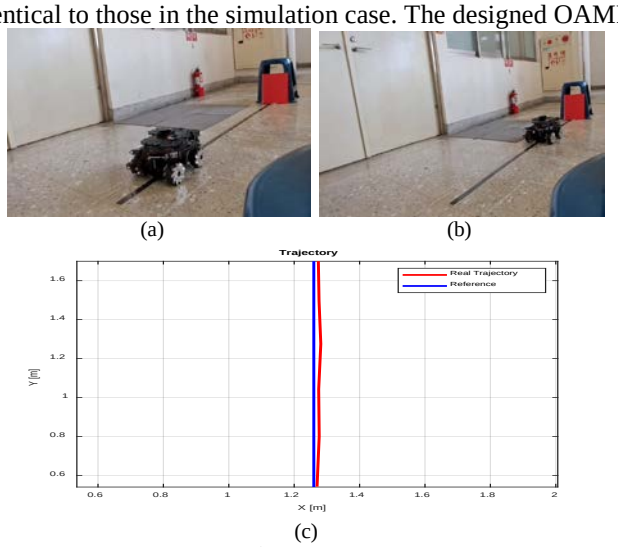

(a) (b)

(c)

Fig. 11. Experimental pictures of the proposed dynamic controller during the experiment. (a)-(b) Two still pictures during the experiment process. (c) Experimental trajectory tracking result of proposed dynamic controller.

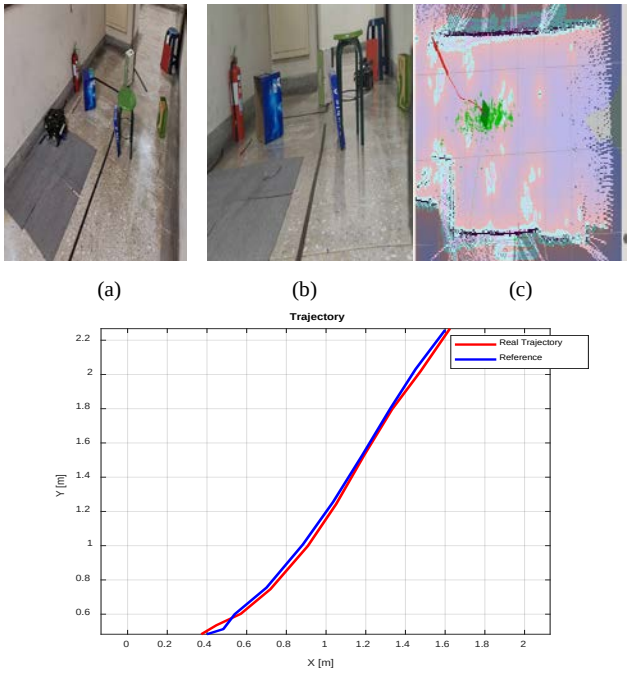

(a) (b) (c)

(d)

Fig. 12. Experimental results of the proposed trackless navigation method. (a)-(b) Two still pictures showing the OAMR movements from its starting point to destination during the experimental process. (c) A glimpse of the OAMR movement using Rviz where the green points denote the particles of the used Gmapping SLAM, the red line represents the planned path to be followed, and the red arrow stands for the destination. (d) Experimental trajectory tracking result of the proposed trackless navigation method.

was utilized to track one slanted line trajectory planned in an

obstacle-free environment. During the experimentation, the OAMR utilized the AMCL for localization and collaborated with the dynamic controller to reach the target position along the black reference trajectory shown in Fig. 11. Figs. 11(a)-(b) depict the two still pictures describing the trajectory tracking results, where the red line denotes the trajectory during the navigation process, and the blue line represents the reference trajectory generated by global path planning. Fig.11(c) shows the tracking results, where the errors could be reduced by using a multi-sensor fusing method in [10]. The results in Fig. 11 demonstrate the effectiveness and applicability of the proposed dynamic controller.

C. Experimental Results of Trackless Navigation

In this subsection, experimental results of trackless navigation in the presence of unexpected static obstacle will be presented and discussed. Fig. 12 presents the obstacle avoidance environment and Fig. 12(c) shows the built map and AMR navigation using Gmapping SLAM in Rviz, where the green points denote the particles of the used Gmapping SLAM, the red line represents the planned path to be followed, and the red arrow stands for the destination. In this environment, the OAMR performed the global path planning using the A* algorithm and integrated the DWA method for obstacle avoidance strategy. Fig. 12(a-b) illustrates the entire process of obstacle avoidance and reaching the target point. In Fig. 12(d), the tracking trajectory of trackless navigation in the obstacle environment was presented, where the blue line represents the reference trajectory generated by global path planning, while the red line shows the actual trajectory during the navigation process. As can be seen in Fig. 12, the trackless navigation dynamic controller with the with the proposed FWNN-BLS compensator not only reached the target point in navigation but also achieved obstacle avoidance and trajectory tracking, confirming the feasibility and superiority of the strategy.

VI. CONCLUSIONS

In this paper, a novel hybrid navigation method for omnidirectional autonomous mobile robots (OAMRs) has been proposed by presenting a PID path controller for magnetically guided tracked navigation and also incorporating a backstepping PI dynamic controllers with a dynamic FWNN-BLS compensator for trackless navigation. The trackless navigation method has used the FWNN-BLS as the online compensator and the dynamic controller has been derived by first designing the kinematic PI controller and then employing backstepping to synthesize the overall dynamic motion controller. The tracked navigation approach has converted the experimental four-wheel OAMR kinematics model into its differential-drive model by setting the equal speeds of both wheels at the same side, and has adopted the PID controller to achieve stable path tracking with satisfactory tracking performance. Through simulations and experimental results, the proposed hybrid navigation has been demonstrated effective, useful and practical in fulfilling hybrid navigation of the experimental OAMRs. Future work would focus on investigate switching policy of the hybrid navigation and conduct more experiments to verify the superiority and practicability of the switching hybrid navigation.

REFERENCES

[1] F. A. X. Da Mota, M. X. Rocha, J. J. P. C. Rodrigues, V. H. C. De Albuquerque, and A. R. De Alexandria, “Localization and navigation for autonomous mobile robots using Petri nets in indoor environments," *IEEE Access, vol. 6, pp. 31665-31676,2018*.

[2] S. Jain, U. Agrawal, A. Kumar, A. Agrawal, and G. S. Yadav, “Simultaneous localization and mapping for autonomous robot Navigation," in *Proc. 2021 International Conference on Communication, Control and Information Sciences (ICCISc)*, 2021: IEEE, pp. 1-5.

[3] P. C. Hsiao and C. C. Tsai, " Autonomous outdoor navigation and driving of a nonholonomic AMR using SVR-based RRT* and model predictive control," in *Proc. of 2024 National Conference on Advanced Robotics* (*NCAR 2024*), National Taiwan University, Taipei, Taiwan, August 22-24, 2024.

[4] Y. L Wang and C. C. sai, " Autonomous behavior-based navigation using fuzzy Kohonen clustering network for differential-drive AMR in partially unknown indoor environments," in *Proc. of 2024 National Conference on Advanced Robotics* (*NCAR 2024*), National Taiwan University, Taipei, Taiwan, August 22-24, 2024.

[5] C. Ju, Q. Luo and X. Yan,, " Path planning using an improved A-star algorithm," in *Proc. 2020 11th Int.Conf. on Prognostics and System Health Management (PHM-2020 Jinan)*, 2020: IEEE, pp. 23-26.

[6] Q. Zhang, L. Li, L. Zheng, and B. Li, " An improved path planning algorithm based on RRT," in *Proc. 2022 11th Int. Conf. of Information and Communication Technology (ICTech))*, 2022: IEEE, pp. 149-152.

[7] N. Y. Allagui, D. B. Halima abid, and N. Derbel, " Fuzzy PI controller for mobile robot navigation and tracking,"in *Proc. 2018 15th Int. Multi-Conf. on Syst. Signals & Devices (SSD)*, 2018, pp. 1178-1183.

[8] C. L. P. Chen and Z. Liu, "Broad learning system: an effective and efficient incremental learning system without the need for deep architecture," *IEEE Transactions on Neural Networks and Learning Systems*, vol. 29, no. 1, pp. 10-24, Jan. 2018.

[9] A. Rospawan, C. C. Tsai, and F. C. Tai, “Adaptive predictive PID control using recurrent fuzzy broad learning system for accurate setpoint tracking of digital nonlinear time-delay dynamic systems,” *Int. J. IRobotics*, vol. 5, no. 3, pp. 26–32, Nov. 2022.

[10] Y. R. Li, *Intelligent adaptive motion control for Mecanum wheeled omnidirectional robots*, Master Thesis, Department of Electrical Engineering, National Chung Hsing University, August 2010.

[11] S. Yilmaz and Y. Oysal, " Fuzzy wavelet neural network models for prediction and identification of dynamical systems," *IEEE Trans. on Neural Networks, vol. 21, no. 10, pp. 1599-1609*, 2010.

[12] K. Sureeya, C. Karupongsiri, and K. Chetpattananondh, “Implementation of a IR sensor as a measurement device for smart farming," *Proc. 2021 18th Int.Conf. on Electrical Engineering/Electronics, Computer, Telecommunications and Information Technology (ECTI-CON)*, 2021: IEEE, pp. 742-745.

[13] J. W. Su, *QPSO-AEKF multisensorial global localization and intelligent hybrid navigation of omnidirectional AMRs*, Master Thesis, Department of Electrical Engineering, National Chung Hsing University, August 2024.

[14] S. Lowry et al, " Visual place recognition: a survey," *IEEE Transactions on Robotics, vol. 32, no. 1, pp. 1-19,2016*.

[15] S. C. Chen and C. C. Tsai, " Monocular depth estimation using YOLOv5 for enhanced BEV mapping in autonomous driving," in *Proc. of 2024 International Conference on Advanced Robotics and Intelligent Systems* (*ARIS 2024*), National Taiwan University, Taipei, Taiwan, August 22-24, 2024.

[16] J. W. Su and C. C. Tsai, “QPSO-AEKF fusing multiple sensors for global localization of omnidirectional AMRs,” in *Proc. of 2024 National Symposium on System Science and Engineering* (*NSSSE 2024*), National Yang-Min Chiao-Tung University, Hsinchu, Taiwan, June 26-28, 2024.

Ching-Chih Tsai received the Diploma in the Department of Electrical Engineering from the National Taipei Institute of Technology, Taipei, Taiwan, in 1981, the M.S. degree in the Institute of Control Engineering from National Chiao Tung University, Hsinchu, Taiwan, in 1986, and the Ph.D. degree in the Department of Electrical Engineering from Northwestern University, Evanston, IL, USA, in 1991. He is currently a Life Distinguished Professor in the Department of Electrical Engineering at National Chung Hsing University (NCHU), Taichung, Taiwan. He served as the Chair of the Department of

Electrical Engineering at NCHU from 2012 to 2014. From 2012 to 2016, he served for two-term President of the Chinese Automatic Control Society (CACS), Taiwan. From 2016 to 2019, he served for two-term President of the Robotics Society of Taiwan (RST). From 2019 to 2021, he served as the President Elect for the International Fuzzy Systems Association (IFSA) and served as the IFSA President from 2021 to 2023. Since 2022, he has served as a BoG member and associate vice president of IEEE Systems, Man and Cybernetics Society, and a BoG member for IEEE Nanotechnology Council. He has served as Dean of College of Electrical Engineering and Computer Science, NCHU, since August, 2024. He has published and co-authored more than 700 technical articles. He received the Outstanding Research Award from the Ministry of Science and Technology, Taiwan, in 2018, and received many awards and recognitions from international conferences supported by IEEE. His current research interests include intelligent control, smart mobile robotics and automation intelligence with their applications to service and industrial robots, semiconductor manufacturing and intelligent machinery. He is a Fellow of IEEE, IET, CACS, RST, and TFSA.

Chi-Hsiang Li received the Diploma degree in Department of Electronic Engineering (Program of Computer Engineering) from the Oriental Institute of Technology, Taipei, Taiwan, in 1991, the B.S. degree in Department of Information Management from Chaoyang University of Technology, Taichung, Taiwan, in 2000, the M.S. degree in Department of Electrical Engineering from National Chung Hsing University, Taichung, Taiwan, in 2017. He is currently pursuing the Ph.D. degree in the Department of Electrical Engineering, National Chung Hsing University, Taichung, Taiwan. His current research interests include pattern recognition, intelligent control, collaborative control of multi-axis motion, BLDC motor driving and their applications to industrial sewing machine control systems.

Chia-Wei Su received his B.S. degree from the Department of Electrical Engineering, National Changhua University of Education, Changhua, Taiwan, ROC, in 2022, and his M.S. degree at the Department of Electrical Engineering, National Chung Hsing University, Taichung, Taiwan, ROC, in 2024. His current research interests include mobile robotics, intelligent control and hybrid navigation.

Shih-Che Chen received the B.S. degree at the Department of Industrial Engineering and Management, I-Shou University, Kaohsiung, Taiwan, ROC, in 2009, and M.S. degree at the Department of Industrial Management, National Pingtung University of Science and Technology, Pingtung, Taiwan, ROC. in 2011. Since 2021, he has been working toward his Ph.D. degree at the Department of Electrical Engineering from National Chung Hsing University, Taichung, Taiwan, ROC. His current research interests include artificial intelligence, intelligent control, computer vision and recognition and their applications to autonomous mobile robots, intelligent industrial robots and machine tools.